HI Balmer Jump Temperatures for Extragalactic HII Regions in the CHAOS Galaxies

A Senior Thesis

Presented in Partial Fulfillment of the Requirements for Graduation *with Research Distinction* in Astronomy in the Undergraduate Colleges of The Ohio State University

By

Ness Mayker

The Ohio State University

April 2019

Project Advisors: Danielle A. Berg, Richard W. Pogge

Table of Contents

Abstract

By understanding the observed proportions of the elements found across galaxies astronomers can learn about the evolution of life and the universe. Historically, there have been consistent discrepancies found between the two main methods used to measure gas-phase elemental abundances: collisionally excited lines and optical recombination lines in H II regions (ionized nebulae around young star-forming regions). The origin of the discrepancy is thought to hinge primarily on the strong temperature dependence of the collisionally excited emission lines of metal ions, principally Oxygen, Nitrogen, and Sulfur. This problem is exacerbated by the difficulty of measuring ionic temperatures from these species. In this work I am exploring an alternative method of estimating nebular temperatures – the H I Balmer recombination continuum jump. Balmer jump temperatures measure the average electron temperature for the entire H II region, rather than only measuring the temperature in the part of the nebula where a particular metal ion is primarily found. Here I present robust measurements of the Balmer jump electron temperature using the best spectra obtained from the CHemical Abundances of Spirals (CHAOS) project. CHAOS has measured elemental abundances in 274 H II regions in 4 spiral galaxies using the Large Binocular Telescope. In this work, I present Balmer temperature measurements in 58 of the CHAOS H II regions and show how they correlate with different ionic temperatures from the same nebulae. In particular, the Balmer temperature correlates best with the ionic temperature derived from the S^{++} emission lines. Determining the best nebular temperature measurement in H II regions has important implications for resolving the abundance discrepancy problem and thus properly calibrating empirical diagnostics of elemental abundances derived from bright collisionally excited emission lines.

Chapter 1: Introduction

If you ask an astronomer what the universe is made up of, you might be surprised to get the response "Hydrogen, Helium, and Metals." Astronomers canonically refer to any element heavier than helium as a metal. On the cosmic scale, the universe is comprised of Hydrogen and Helium, with only trace amounts of metals. The majority of the Hydrogen and Helium we see today was created during the early, hot phases of the Big Bang. Practically all of the elements heavier than Helium are products resulting from the lives and deaths of stars. Figure 1.1 is a version of the periodic table created by Jennifer Johnson (2019) that summarizes the different cosmic sources of elements, originating from events like everyday stellar nucleosynthesis to rare neutron star mergers.

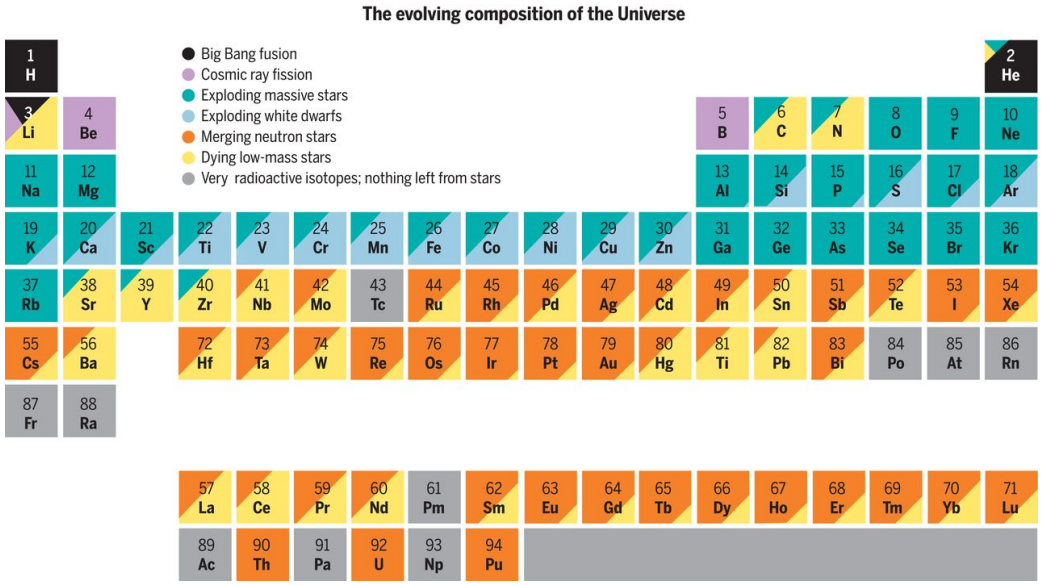

Fig. 1.1.— This variant of the periodic table reveals the cosmic origin of the elements (Johnson 2019).

Astronomers seek to understand the observed proportions of the elements and how they have contributed to the evolution of life and the universe. Studying the chemical composition of our solar system tells us about how our planets have formed, the solar composition informs us about how our sun evolves, and the relative abundances of the elements in the solar system are representative of the chemical abundances of the region of the Milky Way near the sun, as shown in Figure 1.2 (Lodders 2010). Hydrogen, Helium, Carbon, Oxygen, and Nitrogen are among the most abundant elements in the universe. Of these; H, C, O, and N are the primary elements of life on Earth. Identifying different elemental species and their relative abundances across galaxies provides insights into galactic evolution, and allows astronomers to explore the history of a galaxy.

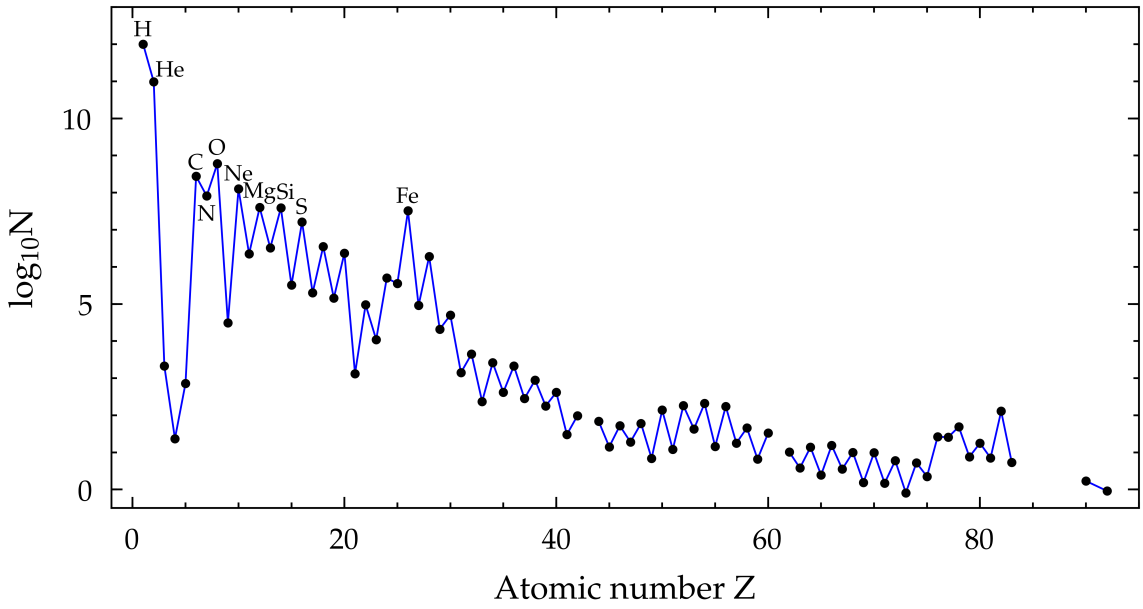

Fig. 1.2.— The relative abundances of the most common elements found in the solar system. Figure from "Stellar Structure and Evolution" Pinsonneault & Ryden (2019), using data from Lodders (2010).

There are a wide variety of ways to measure elemental abundances. Locally we have probed meteorites, analyzed spectra of our sun, and sampled the solar wind. We have explored the chemical composition of our own solar system and have used its make-up to understand its history. Starting with a universe consisting of mostly

Hydrogen and Helium, our existence is based on the metals which have formed as a consequence of stellar and galactic evolution. We seek to better understand where these elements originate from and how they build up over time.

We can step outside of our own solar system and probe the Milky Way, but as we explore out to farther distances the observations become increasingly more challenging. As individual stars become more difficult to resolve, their elemental abundances become harder to measure. Regardless of this, measuring the chemical abundances of nearby spiral galaxies has become an active field in astronomy.

Fig. 1.3.— A composite Hubble Space Telescope image of the spiral galaxy M101. Credit: NASA, ESA, CXC, SSC, and STScI.

Figure 1.3 shows an image of the spiral galaxy M101. Spiral galaxies are dynamic places. Their characteristic spiral arms – outlined by hot, blue, newly-forming stars – contrast with the central stellar bulge which is filled with older and cooler yellow and red stars and dust. Single stars are not apparent in this image, but we can see clusters ranging from hundreds to thousands of stars. Wispy red nebulae are spread throughout the dust lanes. These nebulae, clouds of interstellar gas, are ionized by UV photons by the clusters of newly-formed stars embedded within them. These nebulae are called H II regions because of the presence of ionized Hydrogen, the dominant form of Hydrogen found within them. These large nebulae can be many tens to hundreds of parsecs across, very luminous and therefore readily observed even at large extragalactic distances. Their spectra are characterized by strong emission lines with an underlying continuum composed of starlight and nebular (bound-free and free-free) continuum. Figure 1.4 shows an example of a spectrum from an H II region.

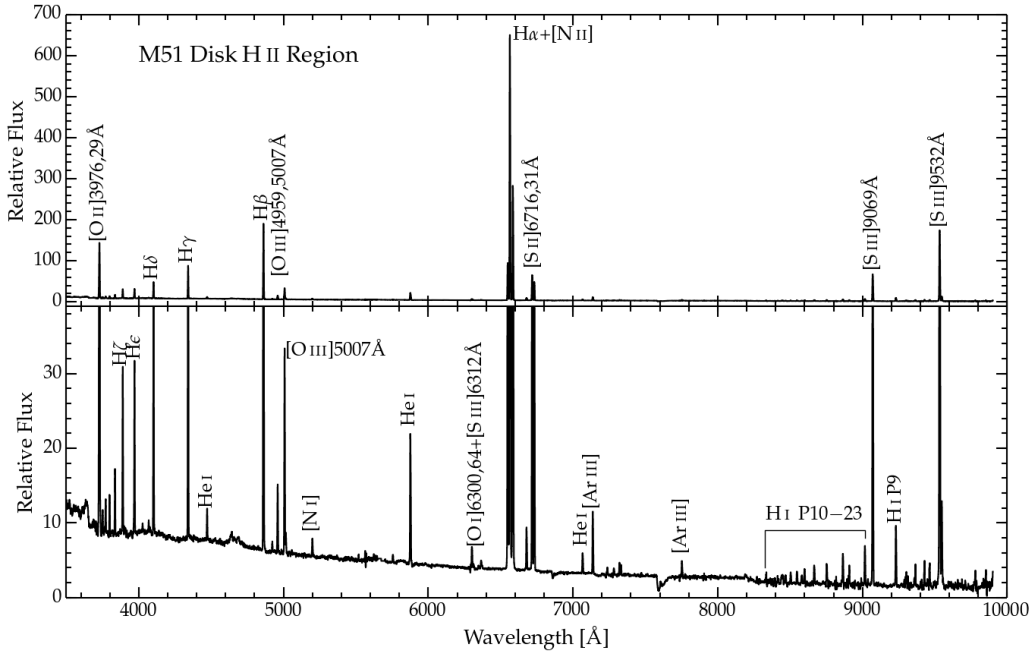

Fig. 1.4.— An example of a spectrum from an H II region. Notice the intensity of the emission lines are much stronger than the underlying continuum. Data from Croxall et al. (2015) [CHAOS Paper 2].

H II regions are heated by photoionization of Hydrogen and other elements by stellar UV photons. Photoionization is balanced by recombination of free electrons with ions of Hydrogen and other elements, with the two processes rapidly achieving a state of photoionization equilibrium. The temperature of the nebula is characterized by the kinetic temperature of the free electrons. These photoelectrically-heated nebulae cool primarily through recombination and electron-ion impact excitation followed by radiation of emission lines as the excited ions relax into the ground state. Although metals exist in much smaller concentrations than Hydrogen and Helium within H II regions, they are responsible for most of the cooling that occurs within the nebula. The excitation energies of the ground states of metals are lower than that of Hydrogen or Helium (few eV compared to 10.2 eV for the first excited state of Hydrogen) and matches more closely with the thermal energy of the free electrons within the region. As shown in Figure 1.5, the metals are more readily excited than the Hydrogen or Helium atoms when a collision occurs, regardless of the temperature of the region.

Because metals function as the primary coolant, the subsequent temperature of the electrons depends critically upon the abundance of metals in the nebulae. The more metals relative to Hydrogen within the nebula, the cooler the nebula will be for the same rate of photoionization heating from the hot stars. This is why even though metals are a minority constituent of the gas ($\sim 1\%$ by mass), they are the dominant source of emission lines in the spectrum, followed by the recombination emission lines of H and He. This feature allows the metal ions to be used as direct probes of the gas-phase abundances in the nebula.

By measuring the abundances of elements in extragalactic H II regions we are able to view a snapshot of the material that the new stars are born from as well as to study the distribution of these elements across the galaxies. These distributions form abundance gradients and enrichment patterns that reveal important clues about the history of the galaxy and allow us to learn about how it has evolved over time.

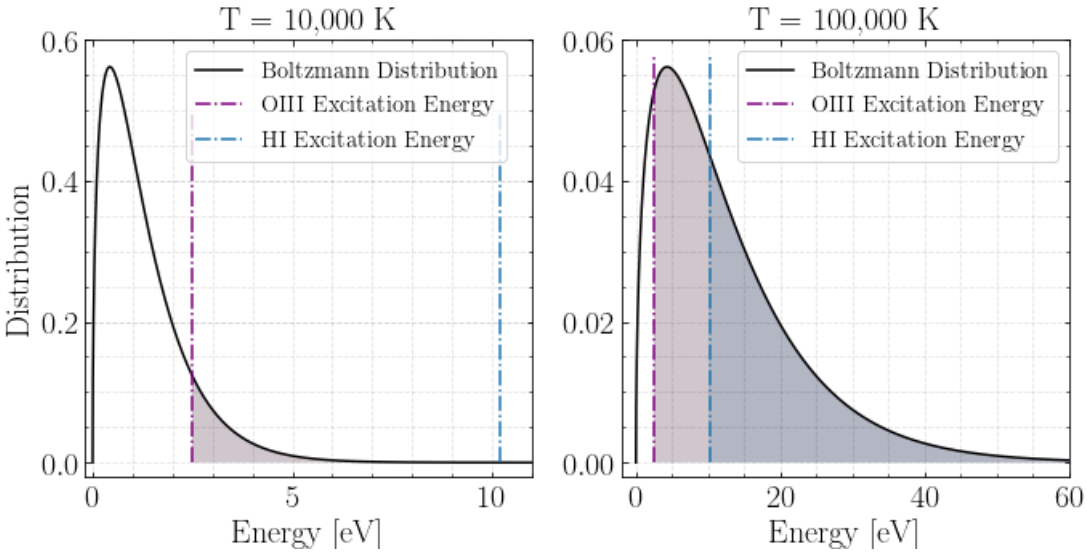

Fig. 1.5.— H II regions have typical temperatures ranging from 5,000 to 15,000 Kelvin. In these regions the distribution of thermal kinetic energy is comparable to the O III (O^{++}) excitation energy; but is not high enough to collisionally excite H I (neutral Hydrogen). However, at sufficiently high temperatures, collisional excitation of H I starts to become important, but the metals will continue to be the main source of cooling.

1.1. Measuring Nebular Abundances

In order to measure elemental abundances, we must first know the thermodynamic properties of the nebular gas, specifically the temperature and density. There are two fundamental physical processes that produce emission lines in an H II region. The first is recombination of ions and free electrons. The intensity of a Hydrogen recombination line such as Hβ ($n = 4 - 2$ transition) is proportional to the integral of the volumetric recombination rate along the line of sight through the nebula:

$$\mathrm{I(H}\beta) = \frac{1}{4\pi} \int_{los} n_e n_p h\nu_{H\beta} \alpha_{H\beta}(T_e)\, ds. \tag{1.1}$$

In this equation n_e and n_p are the number densities of the electrons and protons respectively, hν is the energy of the Hβ emission-line photon, and $\alpha_{H\beta}(T_e)$ is the recombination coefficient for Hβ, the volumetric rate at which recombinations lead

to Hβ emission. The recombination rate depends on the electron temperature in the sense that recombination is more likely at lower temperatures because it is easier to capture slower moving electrons.

Optical recombination lines (ORLs) are more easily observed for abundant elements such as Hydrogen and Helium. Metals such as Carbon, Nitrogen, and Oxygen also produce recombination lines, but they are approximately 10^{-3} to 10^{-4} times weaker than those of Hydrogen, in direct proportion to their abundance relative to Hydrogen. In principle, metal recombination lines should give us an accurate measure of metal abundances, but we can rarely observe them because of how weak they are in the spectra.

The second process that produces emission lines in H II regions is electron-ion impact excitation of metals. The brightest metal emission lines seen in the spectra of H II regions are all collisionally-excited lines (CELs). The intensity of a CEL for a metal ion X is:

$$\mathrm{I(coll)} = \frac{1}{4\pi} \int_{los} n_e n_u(X) h\nu_{line} q_{line}(T_e)\ ds \tag{1.2}$$

In this equation, n_e is the number density of the electrons, $n_u(X)$ is the number density of ion X with an electron in upper excited state u, $h\nu_{line}$ is the energy of the CEL photon, and $q_{line}(T_e)$ is the rate of collisional excitation into the upper state giving rise to the line. The collisional excitation rate is a very sensitive function of temperature:

$$q_{line} \propto \frac{1}{T_e^{1/2}} e^{-\frac{h\nu}{kT_e}} \tag{1.3}$$

Note the much stronger temperature dependence of CELs than what we see in the ORLs: the intensity of CELs is very sensitive to small changes in temperature. In order to convert an observed CEL intensity into an abundance, we must be able to measure the electron temperature accurately in the nebula. To measure a specific ion temperature, we observe multiple emission lines from a given ion and combine them to determine the ratios of different levels of excitation of that ion within the region. Figure 1.6 shows the ground-state configurations of common metal ions found

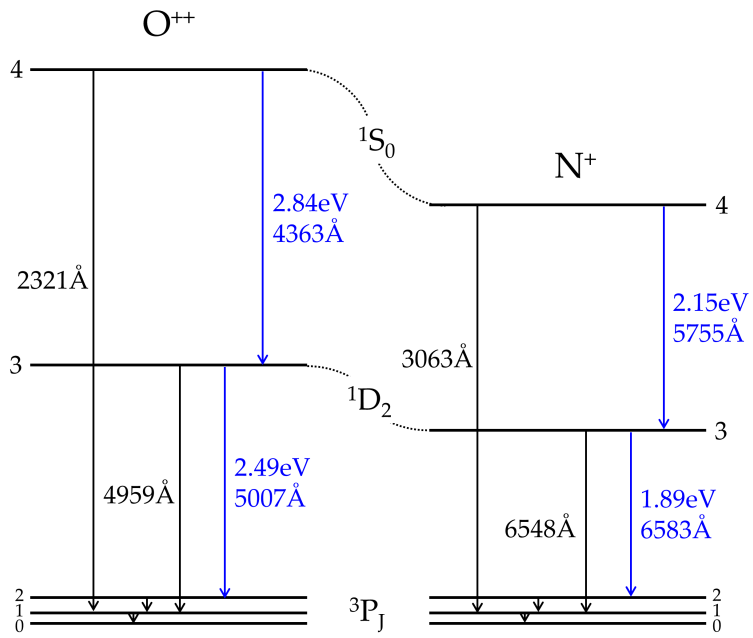

Fig. 1.6.— A comparison of the energy level ground-state configuration in the six-electron ions O^{++} and N^{+}. Notice the different energies necessary to excite electrons and the wavelengths of photons emitted radiatively when the ion de-excites. Image from "Interstellar and Intergalactic Medium" Ryden & Pogge (2016).

in H II regions. When a free electron collides with a metal ion, it excites one of the ion's electrons from the ground state into one of the metastable excited states. Under terrestrial conditions, another free electron collision would follow, and the excited electron would collisionally de-excite out of the metastable state without emitting a photon and the overall kinetic energy of the thermal distribution of free electrons in the gas would remain the same. In H II regions, however, the density of the gas is low enough that the time between collisions is often greater than the time it takes for the electron in the metastable state to de-excite and emit a photon. This is known as a "forbidden transition" because it does not obey the usual dipole selection rules for spontaneous de-excitation: these metastable states are all radiatively de-excited via rare electric and magnetic quadrupole transitions. Before these transitions were understood, astronomers referred to these specific forbidden lines as auroral lines,

because they had only been found within the aurorae in Earth's upper atmosphere. During a forbidden transition the ion spontaneously de-excites, emitting a photon, which carries the excitation energy out of the H II region and into our spectrographs, thus removing energy from the thermal distribution of free electrons and cooling the nebula.

H II regions exhibit ionization stratification (see Figure 1.7), such that the gas closer to the stars is more highly ionized than gas farther out. By measuring the intensity ratios of emission lines produced by different ions, we can measure the electron temperature of that region in which the ions are primarily found. We refer to these regions of stratification as one of three ionization zones (high-, intermediate-, and low-). Within each of these zones are certain ions that are good tracers of the level of ionization; we use the presence of O III to mark the high-ionization zone, S III for the intermediate-ionization zone, and O II or N II for the low-ionization zone. Figure 1.7 illustrates the separation of the different ions within a given H II region.

As we would expect, regions of higher ionization correspond with higher electron temperatures. This is because photoionization raises the kinetic energy of the gas. We expect for our high-ionization zone electron temperatures to be hotter than our ion temperatures indicative of the low-ionization zone, and we expect for our intermediate ionization-zone temperatures to fall somewhere in between.

In some extragalactic H II regions we can measure the auroral lines for most of the ions in the nebula, and see strong correlations from one zone to another as predicted by numerical photoionization equilibrium models. This is because the ionization zones are in thermal contact. This feature is important because sometimes not all of the emission lines of interest are detectable in the spectra of a given H II region. For example, in a very hot region we might only see O III and S III lines and the O II might be too weak to detect. In cases like these, we rely on H II regions in which we observe all of the ion temperatures to derive empirical correlations between the ion temperatures from the different regions. Once we have the ion temperature, we use quantum mechanical models to derive the ionic abundances. The biggest uncertainty of these measurements lies in using the temperature relations when direct temperature measurements cannot be made.

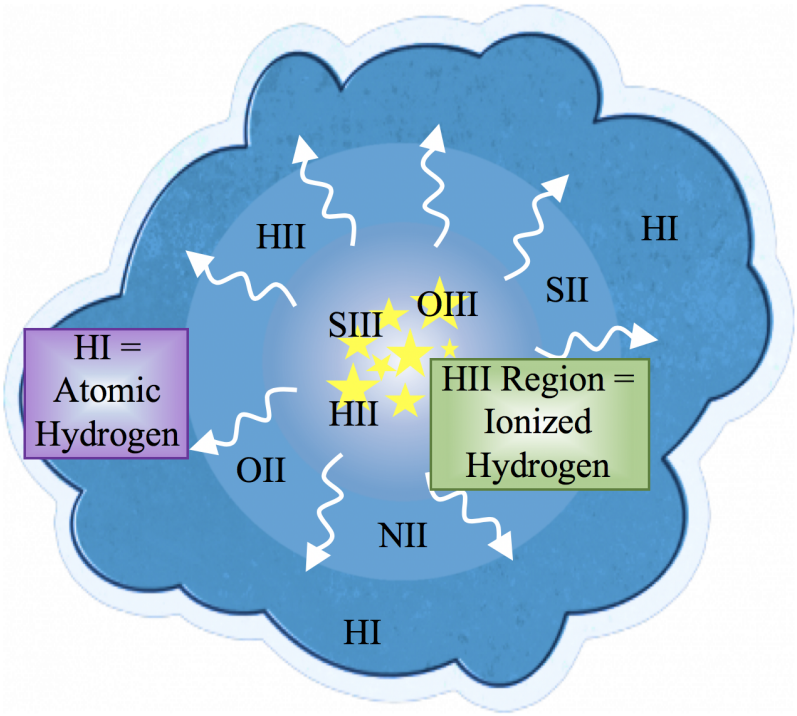

Fig. 1.7.— Each H II region consists of areas of more highly ionized gas surrounded by gas with lower levels of ionization.

For very high S/N spectra we can also use ORL measurements to calculate ion temperatures. For reasons that are still not understood today, there are consistent discrepancies between abundances measured via CELs and ORLs (e.g., Peimbert 1967; Stasińska 2002; Esteban et al. 2004; Peimbert et al. 2005, 2007). Bresolin et al. (2016) explored these discrepancies by comparing the stellar abundances of blue supergiant stars, which should theoretically have the same chemical composition as the H II regions from which they were born. Bresolin showed differing agreement between abundances from CELs and ORLs which depended on the metallicity of the region. They found that for high-metallicity regions, abundances derived from ORLs agreed more closely with the stellar population than the abundances from CELs, whereas this behavior is reversed in low-metallicity regions. In general, the abundances measured via CELs are systematically lower than those measured from ORLs (often referred to as the "abundance discrepancy problem") where although

temperature fluctuations could be partially responsible for the discrepancy, they are not the whole story.

Another difficulty in determining the elemental abundances of H II regions is that although these temperatures are often correlated, we sometimes see very strongly discrepant temperature measurements (Berg et al. 2015), compared to the expectations of photoionization models of nebulae and observed correlations among large samples of H II regions.

We seek to better understand these discrepancies by evaluating the usefulness of each of the specific ion temperatures. Some of the questions worth exploring are: *Is the oxygen temperature too hot? Which temperature is the best indicator of the actual conditions within the nebula?* Due to the inherent challenges in taking these measurements and interpreting the results, we wanted to compare our results to the average electron temperature, or *Balmer temperature*, of the nebula as a diagnostic to help shed light on some of the temperature anomalies we encounter.

1.2. The Balmer Continuum

Recombination of protons (H^+) and electrons occurs throughout the entire nebula. In high S/N spectra we can observe the weak nebular bound-free recombination continuum. When free electrons recombine with protons, a photon is released with energy equal to its kinetic energy plus the binding energy of the recombined electron. Because the kinetic energy is not quantized, the emitted photons will produce a continuous spectrum. This continuum has a break or *jump* at the binding energy of the electron's energy level. The height of the continuum jump is proportional to the energy of the electrons and the temperature of the region.

The Balmer continuum is produced by electrons directly recombining into the first excited ($n = 2$) state of Hydrogen. This continuum is emitted blueward of $\lambda 3646\,\text{Å}$ ($h\nu = 10.2\,eV$) and requires high S/N spectra to be observed. Figure 1.8 shows a spectrum with a strong Balmer continuum component. The discontinuity in the nebular continuum at the Balmer series limit, or the *Balmer Jump*, provides an additional method of independently measuring the electron temperatures in H II

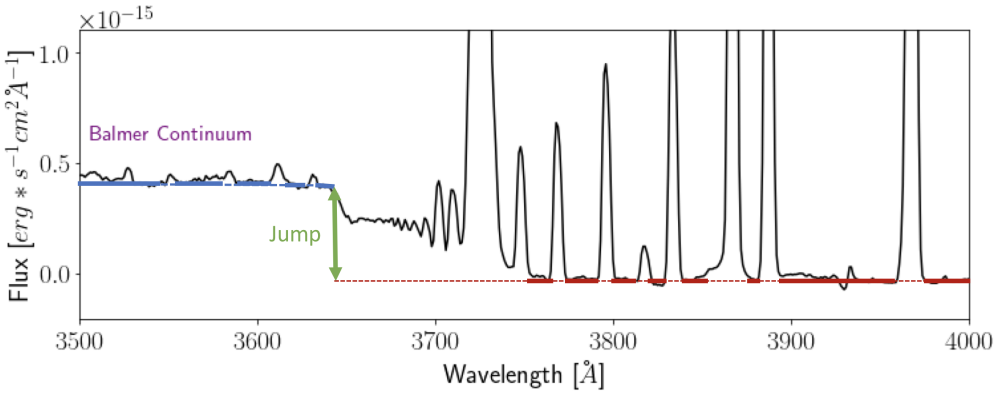

Fig. 1.8.— This spectrum reveals a strong Balmer continuum with a sharp break, also known as the Balmer jump. The Balmer continuum jump is visible in the observed spectrum blueward of λ3646Å and is measured from the difference between the average continuum value blueward of λ3646Å and the underlying continuum redward of λ3646Å. See Section 2.2.2 for measurement details.

regions. A strength of the Balmer Jump method is that, unlike the temperature-sensitive auroral lines, the necessary recombination lines are generally present regardless of the physical conditions within the H II region, and so when viewed in integrated light, it defines a kind of 'average' electron temperature for the entire nebula.

The Balmer Jump was first used by Peimbert (1967) to measure the electron temperature, $T_e(\mathrm{H}^+)$, for 3 H II regions in the Orion nebula complex. Peimbert found that the Balmer temperatures were lower than the temperatures derived from the [O III] λ4363, [O II] λ7320, λ7330, and [N II] λ5755Å auroral lines, largely crediting temperature fluctuations for the differences. Since this pioneering study, the Balmer jump has only been measured in a limited number of nearby galaxies (e.g., Esteban et al. 1998; Garcia-Rojas & Esteban 2006; Guseva et al. 2007) owing, in part, to the need for moderate spectral resolution, high signal-to-noise (S/N), and good blue optical wavelength coverage. See Guseva et al. (2007) for a thorough review of the history of using the Balmer jump to measure electron temperatures.

The work presented here is unique in that the Balmer temperature is used to probe a large sample of low-temperature, high-metallicity H II regions in nearby spiral galaxies. Here, I present Balmer jump electron temperature measurements for 58 H II regions from the CHemical Abundance Of Spirals (CHAOS) survey. The sample and optical spectra are briefly described in Section 2.1. In Section 2.2, I describe the criteria for selecting strong Balmer jump spectra and compare two different methods used to measure the subsequent temperatures. In section 2.3, I show the resulting Balmer jump temperatures using photoionization models in comparison to CHAOS ionic temperatures and provide a summary of our conclusions. Finally, in Chapter 3, I discuss the implications for future work.

Chapter 2: Balmer Jump Temperature in the CHAOS galaxies

2.1. Data

2.1.1. The CHAOS Survey

The CHemical Abundances of Spirals (CHAOS) survey leverages the combined power of the dual 8.4m mirrors on the Large Binocular Telescope (LBT) with the broad spectral range (3200Å $< \lambda <$ 10000Å) and sensitivity of the Multi-Object Double Spectrograph (MODS; Pogge et al. 2010) to measure the physical conditions and abundance gradients of nearby spiral galaxies.

CHAOS seeks to build a large dataset of auroral-line electron temperature measurements of low-temperature, high metallicity H II regions in face-on spiral galaxies. As of this work, 183 H II regions have been analyzed with an unprecedented number of temperature-sensitive CEL detections within these galaxies: NGC 628 (46 H II regions Berg et al. 2015), NGC 5194 (30 H II regions Croxall et al. 2015), NGC 5457 (75 H II regions Croxall et al. 2016)), NGC 3184 (32 H II regions Berg et al. 2019, in prep).

CHAOS optical spectra were acquired using the blue and red channels of MODS on the LBT with the G400L (400 lines mm^{-1}, R$\approx$ 1850) and G670L (250 lines mm^{-1}, R$\approx$ 2300) gratings, respectively. This setup allows for the broad spectral coverage (3200Å $< \lambda <$ 10000Å) needed to measure both the Balmer continuum jump (at λ3646Å) and the temperature-sensitive CEL ratios (e.g., [O III] λ4363/λ5007, [N II] λ5755/λ6584, [S III] λ6312/λ9069). Observations used $2-3$ multi-object field masks for each galaxy in order to obtain spectra from as many H II regions as possible across the galaxy disks.

For a more detailed description of the CHAOS project, see Berg et al. (2015). Here, I describe only the primary points of the data processing. Spectra were reduced and analyzed using the development version of the MODS reduction pipeline which runs within the XIDL reduction package. One-dimensional (1D) spectra were corrected for atmospheric extinction and flux-calibrated based on observations of spectrophotometric flux standard stars (Bohlin 2010).

Spectra of H II regions contain two primary continuum components: underlying starlight and nebular recombination (bound-free) continuum, with starlight the dominant of the two. The stellar continuum is modelled here using the STARLIGHT spectral synthesis code (Fernandes et al. 2005), using the stellar population synthesis models of Bruzual & Charlot (2003). An example of a model stellar continuum plotted with the observed spectrum is shown in Figure 2.1, in which I also plot the resulting nebular continuum revealed by subtracting the stellar component from the observed spectrum. The importance of this step is to isolate the nebular continuum for subsequent measurement free of starlight.

The strength of the nebular emission lines were measured as described in Berg et al. (2015), and were corrected for line-of-sight reddening using relative intensities of the Balmer lines (Hα/Hβ, Hα/Hγ, Hβ/Hγ). The uncertainty associated with each measurement was determined by the combination of the following sources of error: measurement of the spectral variance extracted from the two-dimensional variance image, Poisson noise in the continuum, detector readout noise, Poisson noise from the sky background, flat fielding calibration error, continuum measurement error, and reddening error. An additional 2% uncertainty based on the precision of the adopted flux calibration standards was added in quadrature to the measurement error (see discussion in Bohlin 2010; Berg et al. 2015).

2.1.2. CHAOS Balmer Jump Sample

With the excellent S/N of the CHAOS dataset and blue sensitivity of MODS, many of the spectra in our sample show distinct Balmer continuum jumps. However, in order to make robust measurements of the electron temperatures characterizing our

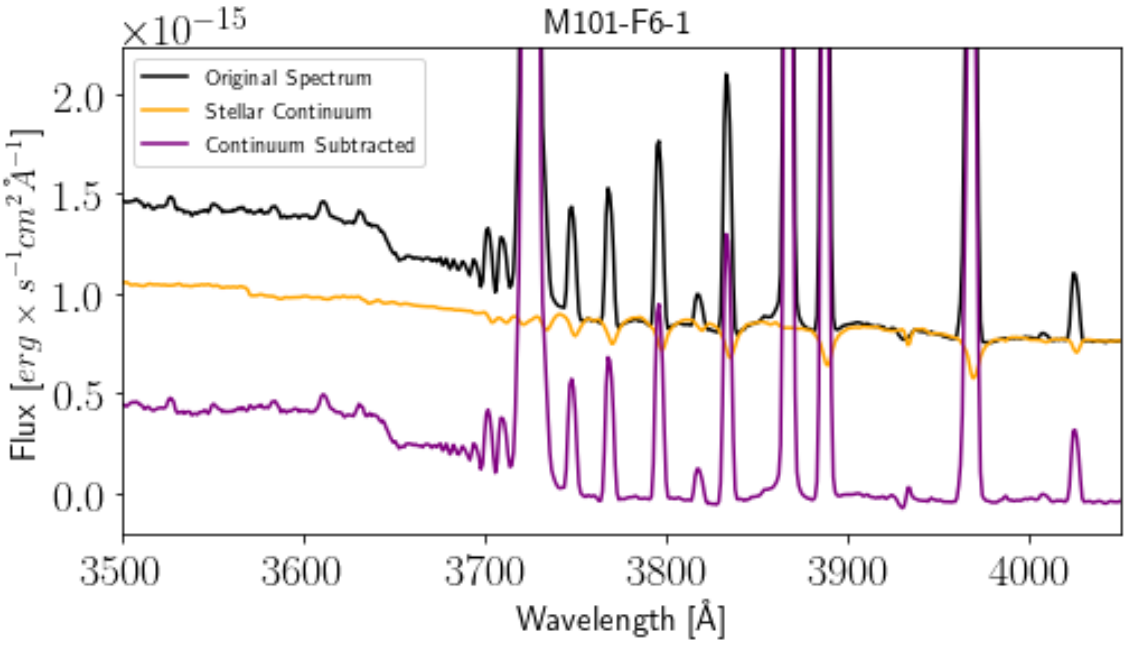

Fig. 2.1.— This figure demonstrates the modelling and subtraction of the stellar continuum component from the observed spectrum. I use the resultant continuum subtracted spectrum for all subsequent analysis of the line and continuum components of the nebular spectrum.

H II regions, I have carefully selected a sample of the 58 highest-quality H II region spectra based on the following criteria:

1. Spectra must have a distinct Balmer continuum jump with a strength that is greater than the S/N of the continuum.

2. Spectra must have one (or more) significant auroral line temperature measurements, allowing the temperatures that probe different ionization zones to be compared to the more globally averaged Hydrogen recombination temperature.

3. Stellar continuum models to the spectra must show negligible stellar Balmer continuum features. This criteria ensures that uncertainties in the stellar continuum fits will not significantly affect the nebular Balmer jump temperature measurements.

The four galaxies reported in the CHAOS project thus far have provided a rich dataset of auroral line temperature measurements, with the H II regions having measurements from *1 or more* ions. We use the above selection criteria to compose a *primary* Balmer jump sample of 27 H II regions from NGC 0628, NGC 3184, NGC 5194, and NGC 5457.

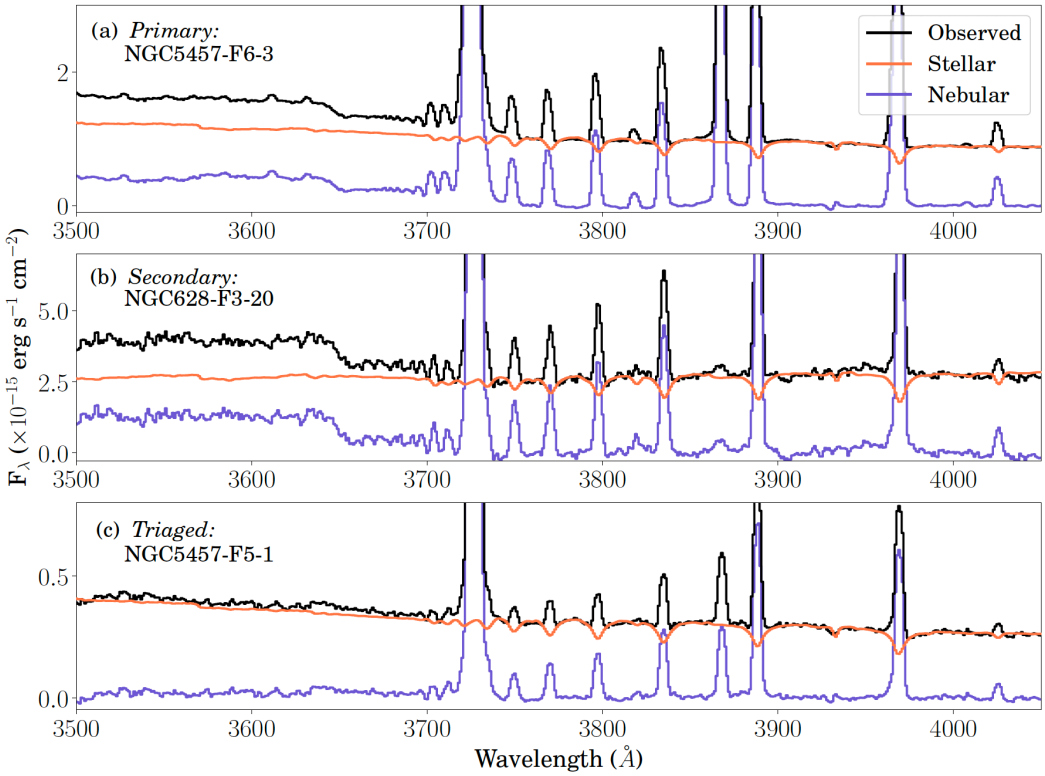

Fig. 2.2.— Top Panel: Example of a Primary Sample high S/N spectra with stellar absorption features that are relatively small compared to the nebular features. Middle Panel: Secondary sample consists of lower S/N spectra with stronger relative stellar absorption features. Bottom Panel: Triaged sample has no visible Balmer jump, low S/N, or relatively high stellar absorption features.

Examples of the types of Balmer continuum discontinuities observed in the CHAOS spectra are shown in Figure 2.2, where a spectrum representative of our *primary* sample is displayed in the top panel. We further designate a *secondary*

Balmer jump sample consisting of spectra that are more representative of the CHAOS dataset as a whole (see the middle panel of Figure 2.2), with 31 H II regions from our CHAOS database. Note that NGC 3184 is composed of mostly low-ionization H II regions that results in Balmer jump measurements for only two H II regions, both of which are in the *primary* sample. Finally, H II regions which did not meet our selection criteria, either having no direct auroral-line temperature measurements or no visible Balmer jump (see bottom panel of Figure 2.2), were removed from our sample and are not discussed further.

2.2. Balmer Jump Temperature Determinations

2.2.1. Balmer Continuum Significance

This work seeks to explore the aspect of the abundance discrepancy problem between CELs and ORLs related to how we measure nebular electron temperatures. By measuring the average electron temperature of the nebula we can determine trends within the regions and better understand any anomalous or discrepant temperature relationships. To do so, we employ the Balmer temperature as an independent method of measuring electron temperatures in H II regions. The Balmer temperature relies on the ratio of a Hydrogen recombination line, such as Hβ or H11, to changes in the nebular continuum across the Balmer series: the *Balmer Jump*.

The nebular continuum is composed of free-bound (recombination), free-free (thermal bremsstrahlung), and two-photon (decay) emission. In the optical wavelength range, Hydrogen bound-free emission is the dominant contributor to the nebular continuum. Aside from Hydrogen, the Helium bound-free emission is the second most significant component of the nebular continuum. The He I continuum is relatively weak compared to Hydrogen, and the He II continuum is only significant when He is doubly ionized, which is uncommon in the relatively cooler temperatures of H II regions. Although free-free emission dominates the nebular continuum in the infrared (IR) and radio wavelengths, its impact on the optical continuum is trivial. Finally, the Hydrogen two-photon process contributes smoothly to the continuous emission, whereas the two-photon emission from He I and He II are generally negligible for nebulae.

The continuum we observe is representative of the average conditions of the region dominated by the H I free-bound recombination spectrum, which manifests as the "Balmer jump" break of the continuum occurring at the limit of the Balmer series at $\lambda 3646$ Å. We can probe this feature to uncover information about the average electron temperature of the nebula. The size of the Balmer jump in an H II region depends on both the temperature and the density. Each of the H II regions within the CHAOS survey are consistent with the low-density limit of (~ 100 cm^{-3}). This results in the Balmer jump as a direct indicator of the average electron temperature of the nebula.

The strength of the Balmer Jump (BJ) is then parameterized as the difference in the nebular continuum intensity blueward and redward of the jump, where BJ $= I_c(\lambda 3646^-) - I_c(\lambda 3646^+)$, as previously shown in Figure 1.8.

2.2.2. Balmer Continuum Measurements

I used a bootstrap Monte Carlo method to fit a linear model to the nebular continuum blueward and redward of the Balmer jump. My technique perturbed the average spectrum by randomly sampling values from the Gaussian probability distribution function characterizing continuum noise in order to generate 1,000 artificial spectra. For each iteration, I modeled the continuum blueward of the jump from $\lambda\lambda$3500-3630Å with a least-squares linear fit, masking regions of potential He I emission (λ3587.00, λ3613.60, and λ3634.24Å). The continuum redward of the jump was fit in a similar manner, using the nebular continuum from $\sim\lambda\lambda$3750-4050Å, but avoiding strong emission features such as [O II] λ3727Å, H I Balmer and He I lines (e.g., λ3727, λ3770.63, λ3797.90, λ3819.61, λ3835.39, λ3868.75, λ3889.05Å). These red windows are identical to those used to model the stellar continuum with STARLIGHT (see Section 2.1.1). Due to the limited resolution of the MODS spectra and the close spacing of the Balmer emission lines $\lesssim \lambda$3750Å, the nebular continuum is not resolved from $\lambda\lambda$3646-3757Å and for this reason I do not use this spectral window in the Balmer continuum fitting. An example of the resulting best blue and red continuum fits is shown in Figure 2.3, where the overall fits are marked with blue and red dashed lines, respectively, and the continuum windows used in the fitting are designated by solid lines.

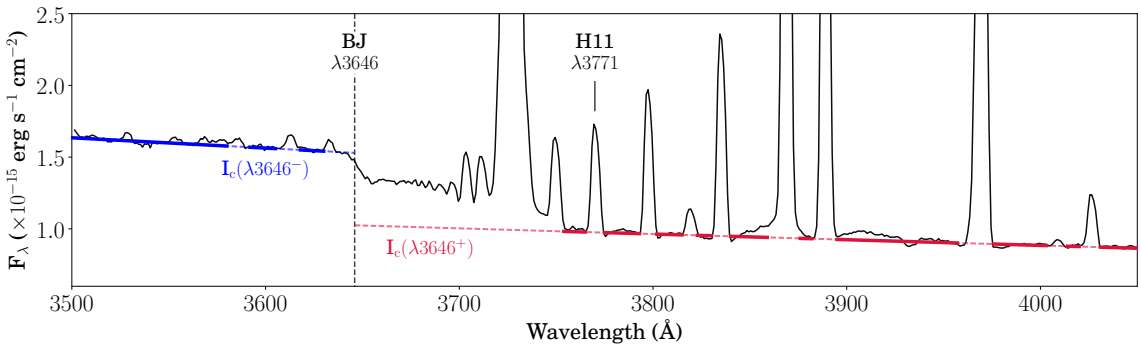

Fig. 2.3.— Measurement of the Balmer jump for the continuum-subtracted spectrum of NGC5457-F6-3 from our primary sample demonstrating our fitting procedure. The best fit blue and red continuum models are shown, along with the H11 emission line used to define the Balmer jump ratio.

The resulting fits were used to measure the BJ by evaluating the nebular continuum blueward of the jump and redward of the jump (measured at λ3643 Å and λ3681 Å respectively). We used the York Extinction Solver (McCall 2004,YES) and the Cardelli et al. (1989) reddening law to estimate the wavelength-dependent extinction coefficients, A_λ, applying $A_v = 3.1 \times E(B-V)$, to reddening correct our jump measurement values and H11 fluxes.

Extinction values were published in the previous CHAOS papers (Berg et al. 2015; Croxall et al. 2015, 2016) as $c_{\mathrm{H}\beta}$, where $c_{\mathrm{H}\beta} = 1.43 \times E(B-V)$. We then define the Balmer jump ratio (BJR) in Equation 2.1: where we determine the relative strength of the Balmer jump to the H11 Balmer line. Measuring this ratio allows for a normalization of the Balmer jump across many spectra, comparing their values to those of the nearby H11 Balmer emission line that is not strongly influenced by the temperature of the region.

$$\mathrm{BJR} = \frac{I_c(\lambda 3643) - I_c(\lambda 3681)}{I(\mathrm{H11})}. \tag{2.1}$$

The small wavelength difference between the Balmer jump and H11 minimizes systematic uncertainty due to flux calibration and the reddening estimates. Balmer jump errors were derived from the standard deviation of posterior distribution from

the Monte Carlo fits, and were combined in quadrature with the H11 flux uncertainties reported in the CHAOS papers.

2.2.3. $T_e(H^+)$ Calculations

I have measured the Balmer temperatures in a large sample of metal-rich extragalactic H II regions. Previous studies have used a variety of methods to measure the Balmer temperature in planetary nebulae (e.g., Peimbert 1971; Barker 1978; Liu & Danziger 1993) and in metal-poor blue compact dwarf (BCD) galaxies (Hägele et al. 2006; Guseva et al. 2007). Notably, Guseva et al. (2006, 2007) used a Monte Carlo technique with a grid of model spectral energy distributions to fit the Balmer jump in spectra of BCDs, however this was only possible due to the combination of resolution and high S/N in their high surface-brightness spectra. Alternatively, Liu et al. (2001, hereafter L01) introduced a simple exponential relationship between the Balmer jump and the electron temperature found in planetary nebulae:

$$T_e = 368 \times (1 + 0.259 \cdot y^+ + 3.409 \cdot y^{++}) \times (\mathrm{BJR})^{-3/2} \tag{2.2}$$

This relation incorporates photoelectron contributions from ionized Helium ($y^+ = He^+/H^+$ and $y^{++} = He^{+2}/H^+$) in planetary nebulae. By comparison, the He^+ contribution is relatively small in an H II region, and the fraction of doubly ionized He is negligible. Even considering the metallicity dependence of y^+, where y^+ ranges from the primordial value (~ 0.085, Aver et al. 2015) at low metallicity to roughly solar (~ 0.100 for Orion, Esteban et al. 2004), y^+ only varies by $\sim$15% over the entire range in oxygen abundance covered by H II regions in our sample. Therefore, for the purposes of this study, I adopt a typical value of $y^+ = 0.0925$.

All studies to date have calibrated their Balmer jump temperature methods using nebulae that are different than the CHAOS H II region sample which extend to higher abudance and lower electron temperatures. In order to determine $T_e(H^+)$ for these H II regions, I used photoionization modeling to derive new Balmer temperature relations appropriate to the parameter space of the sample. I describe the details of these models in the following section.

2.2.4. Photoionization Models

The photoionization modeling used to determine the relationship between the Balmer jump and the average electron temperature of H II regions in the CHAOS sample was outside of the scope of this thesis, yet played an important part of my results and the paper we are preparing for publication. The modeling and analysis of this section was performed by my advisor, Danielle Berg. In this following section, I am presenting her models and the corresponding theory used to derive my resulting Balmer temperatures.

In order to enhance the utility of the rich CHAOS dataset, we sought an improved $T_e(H^+)$ equation that only depends on quantities that are directly measured and readily available (i.e., no y^+ or y^{++}), and that is calibrated over our observed parameter space. Therefore, we created a grid of photoionization models using CLOUDY 17.00 (Ferland et al. 2013) with parameters customized for the CHAOS dataset. Because we are targeting individual, star-forming H II regions that are dominated by their current burst of star formation, we chose to run the CLOUDY models with single-burst stellar population, taken from the "Binary Population and Spectral Synthesis" (BPASSv2.14; Eldridge & Stanway 2016; Stanway et al. 2016) models, for the input ionizing radiation field.

We ran a variety of models in order to cover parameter space appropriate to our sample. Ages of $t = 10^{6.0},\ 10^{6.7}$, and $10^{7.0}$ yrs, which are typical of bright H II regions, were used. A broad range in ionization parameter and metallicities were included, covering $-4.0 < \log U < -2.0$ and ($Z = 0.001, 0.002, 0.004, 0.008, 0.014, 0.020, 0.040 = 0.05, 0.10, 0.20, 0.40, 0.70, 1.0, 2.0\ Z_\odot$), where the same metallicity was assumed to characterize both the stars and the gas. Abundances were initialized with the standard set of GASS10 solar abundance ratios within CLOUDY and scaled to the desired model metallicity. Electron densities from $10^2 - 10^3$ cm^{-3} were also considered. Note that both binary and single-star populations were initially considered, however, we found no dependence on binarity for the Balmer jump temperature, therefore we only discuss the results of single-star population models hereafter.

The model H^+ temperature was set to the radially-averaged $T_e(n_e n_p)$ value at each grid point. We determined the model BJR measurements using the same method employed for our CHAOS observations. Specifically, the BJR was determined by subtracting the modeled nebular continuum measured at λ3643Å and λ3681Å then dividing by the output H11 flux. Both dust-free and dusty models were run, where abundances were depleted following the relative element depletions for Orion. However, the close proximity of the BJ and H11 in wavelength minimizes the effects of dust on the BJR. Further, the intrinsic relationship between the Balmer jump and the H^+ temperature is desired, and so dust-free models were employed for the model BJ measurements.

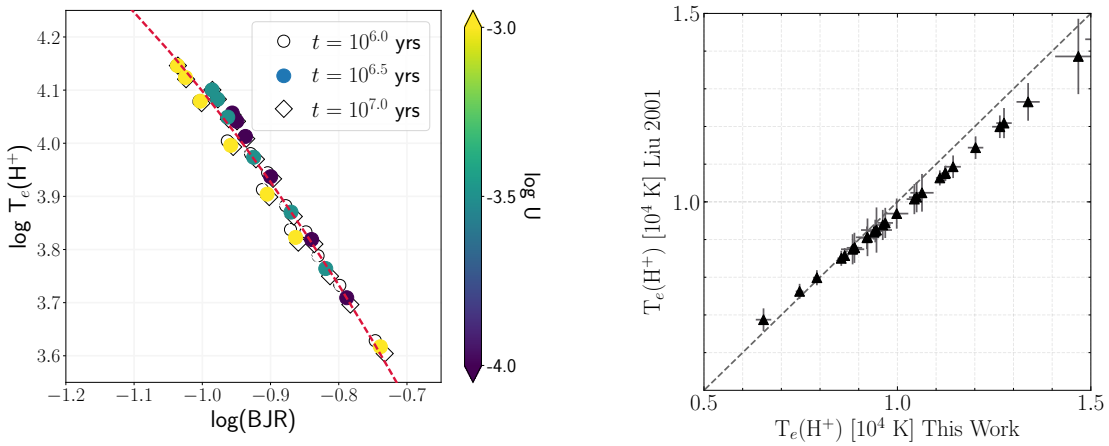

Fig. 2.4.— Left: Balmer temperature as a function of our Balmer jump ratio (BJR) from CLOUDY models of H II regions with a range of ionization parameter ($\log U$) and starburst age (t). Right: comparison of Balmer temperature from this work with the planetary nebula Balmer temperature relation of L01.

The resulting BJRs and H^+ temperatures from the models are plotted in the left panel of Figure 2.4. While relatively small differences in $T_e(H^+)$ versus BJR are seen for different H II region ages, the relationship is clearly rather sensitive to ionization parameter, $\log U$. As expected, the H^+ temperature is inversely related to the BJR; in the sense that higher temperatures have smaller Balmer jumps.

In the right panel of Figure 2.4 we compare our model $T_e(H^+)$ values with the L01 power law prescription based on planetary nebulae (Equation 2.2). Compared to the one-to-one dashed line, we find good agreement with the L01 models for regions of low ionization parameter ($-3.0 \lessapprox \log U \lessapprox -4.0$). However, the L01 model significantly overpredicts the H^+ temperatures for nebula with large ionization parameters ($\log U > -3.0$). While the L01 prescription is reasonable for planetary nebulae, this exercise confirms our intuitions that new models are needed to accurately determine the Balmer jump temperatures for H II regions, especially given the broad range of ionization parameters and conditions covered by the CHAOS dataset.

From our CLOUDY models in Figure 2.4 it is evident that the relationship between $T_e(H^+)$ and BJR is better characterized as a second-order polynomial in $\log(BJR)$ given by Equation 2.3, where $x = \log(BJR)$.

$$\log T_e(H^+) = -1.1484 \cdot x^2 - 3.8927 \cdot x + 1.3540 \tag{2.3}$$

The Balmer temperatures for each region are reported in Tables 2.1 and 2.2 at the end of Chapter 2. All errors were determined using standard error propagation.

2.3. Results

2.3.1. $T_e - T_e$ Relationships

A principal question of this work is whether the standard ionic temperatures measured from auroral lines are good measures of the nebular temperature as a whole, or whether they significantly bias direct metallicity abundances. The answer to this question has implications for the abundance discrepancy problem. This motivated the selection of only the H II regions with many direct auroral line measurements.

In this work we have measured the Balmer continuum jump as an alternative method to determine the typical electron temperature because it samples the entire ionized nebulae. To assess the discrepancies between temperatures in different ionization zones and the average H^+ temperature, we plot our measured $T_e(H^+)$ values versus the [O III], [S III], and [N II] ionic temperatures for the primary sample in Figure 2.5. The three panels show the H^+-to-ionic temperature comparison for the high-, intermediate-, and low-ionization zones, respectively, where the [S III]

intermediate zone temperatures appear to trace the H^+ temperatures the best. We used a Bayesian linear regression model to quantify the relationship between

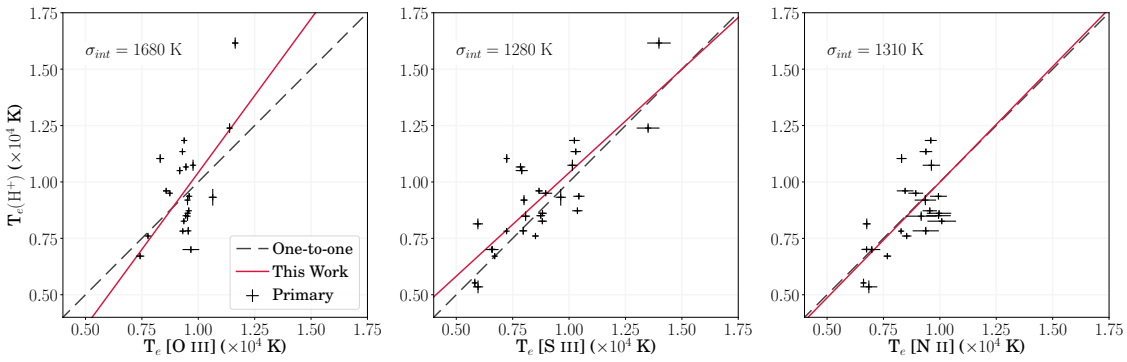

Fig. 2.5.— Balmer jump temperatures, $T_e(H^+)$, compared with auroral temperature measurements for the Primary sample, where T_e[O III], T_e[S III], and T_e[N II] represent the temperatures of the high-, intermediate-, and low-ionization zones of the H II region. Each trend is fit with a Bayesian linear mixture model (solid red line) and compared to the one-to-one relationship (dashed black line). Total and intrinsic dispersions are given in the upper left corner for each fit.

$T_e(H^+)$ and the CHAOS ion temperatures. We adopted the linear mixture model algorithm developed by Kelly (2007) implemented in the python module LINMIX. This method explicitly takes into account errors on both temperatures and allows for intrinsic scatter in the data, which is due to the naturally occurring dispersion in the temperature measurements within the H II regions. This scatter variable is applied to the weighting of each data point and allows us to analyze how much of the dispersion of our data is due to the intrinsic scatter of the H II regions. We found our best fits to be as follows:

$$T_e(H^+) = (1.138 \pm 0.388) \times T_e[\mathrm{OIII}] - (0.099 \pm 0.367), \tag{2.4}$$

$$T_e(H^+) = (1.178 \pm 0.273) \times T_e[\mathrm{NII}] - (0.134 \pm 0.234), \tag{2.5}$$

$$T_e(H^+) = (0.302 \pm 0.104) \times T_e[\mathrm{SIII}] + (0.192 \pm 0.122). \tag{2.6}$$

We find good general agreement between our Balmer continuum jump temperatures, $T_e(H^+)$, and CHAOS ionic temperatures. We have intrinsic scatter

of σ_{int} = 1680K for T_e[O III], 1280K for T_e[S III] and 1310K for T_e[N II]. $T_e(H^+)$ has the least intrinsic scatter when plotted against T_e[S III]. $T_e(H^+)$ measurements have a similarly low scatter when plotted against T[N II], but they do not span as wide of a temperature range. We find $T_e(H^+)$ to have better agreement with T_e[O III] and T_e[N II] at lower temperatures and T_e[S III] at higher temperatures. In

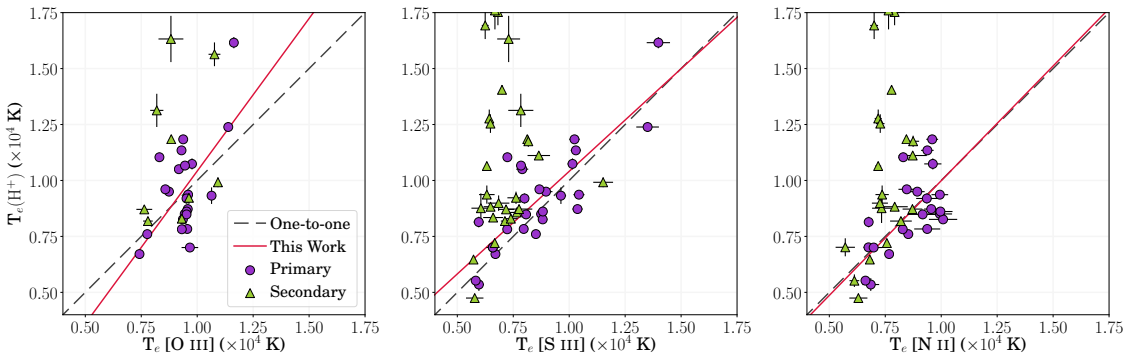

Fig. 2.6.— Balmer jump temperatures, $T_e(H^+)$, compared with auroral temperature measurements, same as Figure 2.5 but with the addition on the Secondary sample. The secondary sample is highly scattered to higher $T_e(H^+)$ values, likely due to the lower S/N of the spectra in the Balmer continuum region.

Figure 2.6 we repeat the plot of $T_e(H^+)$ versus auroral temperature measurements from Figure 2.5 (purple circles), with the addition of the Secondary sample (green triangles). In general, the Balmer jump temperatures of the Secondary sample have a large dispersion that is biased to high temperatures. We can see from our sample, that including our secondary set does not give us reliable information about conditions within the nebula. For this reason, we suggest only using high S/N "primary" spectra to make the Balmer jump temperature measurements.

2.3.2. Discussion

Historically, the [O III] λ4363Å emission line has been considered the "gold standard" for measuring nebular electron temperatures (Maiolino & Mannucci 2019). However, Binette et al. (2012) reported discrepancies between [O III] and [S III] temperatures where none were expected from photoionization models. CHAOS saw

similar discrepancies in a subset of its H II regions that could not be explained as measurement error because of the high quality of the data (Berg et al. 2015). This motivated the CHAOS team to pursue this question further, for example in the study of M101 (Croxall et al. 2016).

The CHAOS analysis of H II regions found that while there was often a discrepancy between T_e[S III] and T_e[O III], they found unexpectedly good agreement between T_e[N II] and T_e[S III] (Berg et al. 2015), and revised the temperature-temperature relations of Garnett (1992) using the high-quality CHAOS M101 spectra (Croxall et al. 2016). One particular result of these studies is that it appears that S III temperatures give more consistent results than O III temperatures.

My results presented here show a low dispersion for the $T_e[S\,\mathrm{III}] - T_e[H^+]$ correlation seen in the middle panel of Figure 2.5. This supports the idea that $T_e[S\,\mathrm{III}]$ rather than $T_e[O\,\mathrm{III}]$ is the fundamental ionic temperature indicator in H II regions, and suggests a possible path forward to resolving the abundance discrepancy problem.

Region	$T_e(H^+)$	T_e[O III]	T_e[N II]	T_e[S III]
M101-F1-4	8000±200	7400±200	7700±200	6900±100
M101-F3-1	9500±100	8700±100	8900±300	9000±300
M101-F3-3	7500±100	7800±100	8500±200	8900±100
M101-F3-9	9100±100	8600±100	8500±400	8700±200
M101-F4-3	13100±200	11400±100	10700±1100	13500±500
M101-F4-4	13700±300	11600±100	10600±1400	14000±500
M101-F4-5	12000±200	9600±100	9900±400	10400±200
M101-F4-6	9800±200	9600±100	9600±300	10300±200
M101-F4-7	11100±100	9400±100	9600±300	10200±200
M101-F4-8	11200±100	9300±100	9400±300	10300±200
M101-F4-9	9700±300	9800±100	9600±400	10100±200
M101-F6-1	8900±100	9400±100	9900±500	8700±200
M101-F6-2	7900±100	9400±100	10100±600	8800±200
M101-F6-3	8300±100	9500±100	10000±500	8800±200
M101-LS1b-1	11600±200	9200±100	···	7900±300
M101-LS1b-3	11400±200	9500±100	9300±900	7800±200
M101-LS1c-1	8500±200	9500±100	9200±700	8100±200
M101-LS1c-2	9600±200	9600±100	9400±600	8000±200
M101-LS1c-3	8100±700	9500±100	9400±500	8000±200
NGC628-F1-22	9400±400	10600±200	···	9600±200
NGC628-F2-22	7800±100	9300±100	8300±100	7200±100
NGC628-F3-15	10000±300	8300±200	8300±200	7200±100
NGC628-F3-20	5500±400	···	6900±400	6000±200
NGC3184-F1-6	7000±300	···	6800±200	6600±100
NGC3184-F2-5	7000±100	9700±400	7000±400	6600±300
NGC5194-F2-20	8100±200	···	6800±200	6000±200
NGC5194-F2-21	5500±200	···	6600±100	5800±100

Table 2.1. Balmer and CEL Temperatures – Primary Sample

Region	$T_e(H^+)$	T_e[O III]	T_e[N II]	T_e[S III]
M101-F2-3	8000±300	7600±400	7900±900	7200±300
M101-F2-6	5500±200	···	6300±400	5800±400
M101-F2-7	2600±100	···	5914±723	···
M101-F3-11	11300±200	···	8700±600	8600±500
M101-F4-1	16200±400	11000±100	···	11500±400
M101-F4-18	9500±600	10800±300	···	···
M101-F5-1	9800±400	9600±100	9100±900	7600±400
M101-F5-11	7900±300	···	···	7700±500
M101-F5-12	10000±300	···	7900±600	6500±300
M101-F5-13	9200±200	···	7800±800	6600±400
M101-F5-20	9500±300	···	8700±400	7800±600
M101-F6-22	7500±100	7800±200	8200±500	7100±200
M101-LS1a-2	7100±200	9300±100	9100±800	7400±300
NGC628-F1-3	12800±400	···	7200±200	6400±100
NGC628-F1-7	17900±600	···	7900±500	6800±200
NGC628-F2-2	7100±200	···	7600±100	6700±100
NGC628-F2-4	10700±200	···	7200±100	6300±100
NGC628-F2-8	9700±200	8800±100	8400±100	8100±100
NGC628-F2-11	13800±500	···	8700±300	8200±100
NGC628-F2-18	13800±200	···	7800±100	7000±100
NGC628-F2-19	6300±100	···	6800±100	5700±100
NGC628-F3-5	16500±1000	8800±600	9100±900	7300±500
NGC628-F3-6	13100±700	8200±300	···	7800±600
NGC628-F3-9	8800±700	···	7300±400	6100±400
NGC628-F3-16	17500±260	···	7600±400	6700±500
NGC628-F3-22	13300±1000	···	7300±200	6500±100
NGC5194-F1-4	5500±300	···	6100±200	···
NGC5194-F1-15	7000±400	···	5700±400	···
NGC5194-F1-18	9000±300	···	7300±400	6800±500
NGC5194-F2-22	9300±400	···	7400±300	6300±300
NGC5194-F3-21	16900±600	···	7000±200	6200±200

Table 2.2. Balmer and CEL Temperatures – Secondary Sample

Chapter 3: Conclusions and Future Work

This project began as the attempt to answer a simple question: *Can the Balmer jump be used to calculate a temperature indicative of the average electron temperature of an H* II *region, and if so, what relationships will that temperature have with the more commonly used ionic temperatures?*

I originally calculated the Balmer temperatures using the L01 equation and although my results were reasonable I expected there would be a slight offset due to the differing characteristics between H II regions and the planetary nebulae the equation was originally modelled after. The next step was to better model the physics of H II regions using photoionization models that were built on the specific parameters of the CHAOS sample.

The first run of models gives results that are consistent with expectations, but the model is relatively simple. For example, it does not include second order effects due to different ionization conditions; some of the CHAOS H II regions are higher ionization than assumed by the models. The next step will be to make more sophisticated models that will explore the effects of different levels of ionization from region to region.

Questions for future work:

1. Some individual H II regions do not follow the temperature correlations, are these due to second order effects, such as ionization state, unaccounted for in our current models?

2. The nebular continuum is the residual left after subtraction of an underlying starlight continuum model. Is there a way to model the nebular and stellar continuum simultaneously?

3. Do all galaxies show the same correlations between Balmer and ionic temperatures?

4. Can the Balmer temperature be used to improve abundance measurements?

Acknowledgements

This work was made possible by support from the Summer Undergraduate Research Program at The Ohio State University Department of Astronomy.

This thesis research was supported in part by grants AST-1108693 and AST-1715284 from the US National Science Foundation, which funded the original CHAOS survey and this subsequent project.

This work has made use of NASA's Astrophysics Data System Bibliographic Services and the NASA/IPAC Extragalactic Database (NED), which is operated by the Jet Propulsion Laboratory, California Institute of Technology, under contract with the National Aeronautics and Space Administration.

This work was based in part on observations made with the Large Binocular Telescope (LBT). The LBT is an international collaboration among institutions in the United States, Italy and Germany. The LBT Corporation partners are: the University of Arizona on behalf of the Arizona university system; the Istituto Nazionale di Astrofisica, Italy; the LBT Beteiligungsgesellschaft, Germany, representing the Max Planck Society, the Astrophysical Institute Potsdam, and Heidelberg University; the Ohio State University; and the Research Corporation, on behalf of the University of Notre Dame, the University of Minnesota, and the University of Virginia.

This paper uses data taken with the MODS spectrographs built with funding from NSF grant AST-9987045 and the NSF Telescope System Instrumentation Program (TSIP), with additional funds from the Ohio Board of Regents and the Ohio State University Office of Research.

This paper made use of the modsIDL spectral data reduction reduction pipeline developed in part with funds provided by NSF Grant AST-1108693 and a generous

gift from OSU Astronomy alumnus David G. Price through the Price Fellowship in Astronomical Instrumentation.

This work made use of the following software packages:

Astropy: a community-developed core Python package for Astronomy (Astropy Collaboration et al. 2013; Price-Whelan et al. 2018) (astropy.org)

CLOUDY: Photoionization Modelling Code (Ferland et al. 2013) (nublado.org)

Jupyter: Notebooks for Python (jupyter.org)

linmix: A Bayesian Linear Mixture Model (Kelly 2007) (github.com/jmeyers314/linmix)

Matplotlib: a 2D graphics package used for Python (Hunter 2007) (matplotlib.org)

modsIDL: Spectral data reduction for the Multi Object Double Spectrographs (Croxall & Pogge 2019) (github.com/rwpogge/modsIDL)

Pandas: Data Structures for Statistical Computing in Python (McKinney 2010) (pydata.org)

Scipy: Open Source Scientific Tools for Python (Jones et al. 2001–) (scipy.org)

STARLIGHT: Stellar Spectral Synthesis Code (Fernandes et al. 2005) (starlight.ufsc.br)

XIDL: an IDL Astronomical Data Reduction Package (github.com/profxj/xidl)

I am grateful for the support from my advisors, Danielle Berg, Rick Pogge, and Don Terndrup, who have provided countless advice on both how to perform and present research.

I am also grateful for the support from my family: Amelia Ebright Mayker (age 2.5), who helped bring artistic inspiration to this work (see Figure 3.1), Draylen Sizemore (age 14), who served as editor and general grammar police, and Robb Ebright, who has dedicated the last few years to child rearing so that I can follow my dream to pursue a career in Astronomy research.

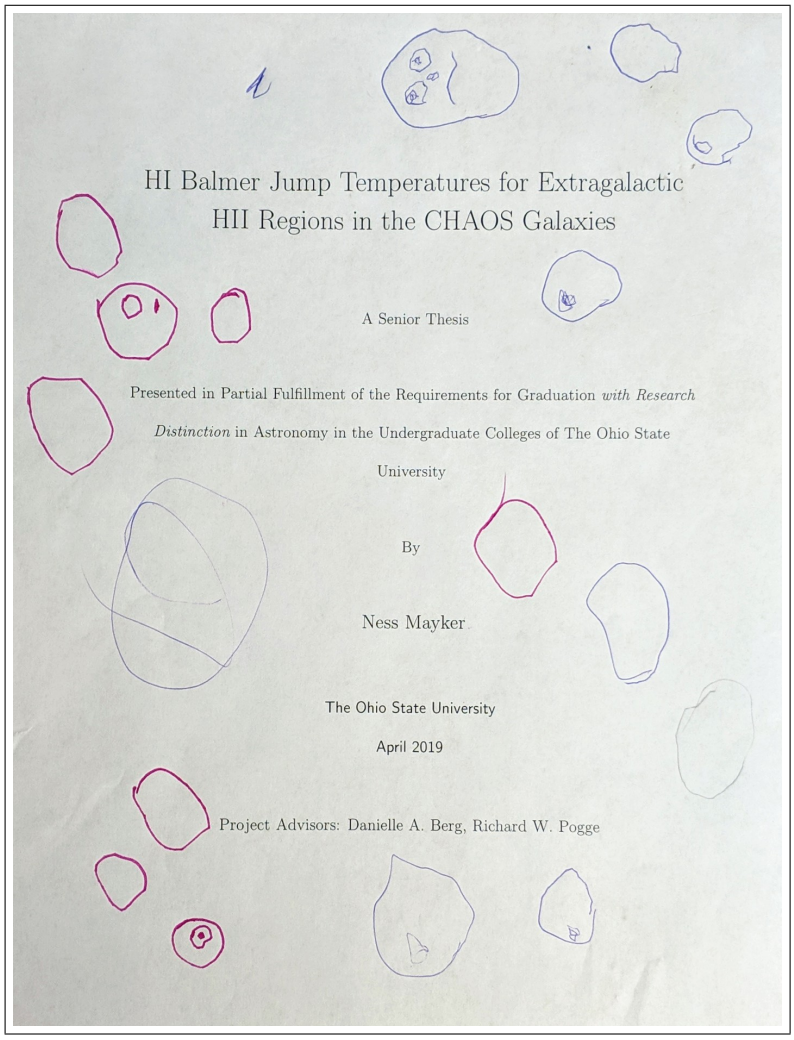

Fig. 3.1.— Artistic rendition of H II regions by Amelia Jane Tethys Ebright Mayker

References

Astropy Collaboration, Robitaille, T. P., et al. 2013, A&A, 558, A33

Aver, E., Olive, K. A., & Skillman, E. D. 2015, , 7, 011

Barker, T. 1978, ApJ, 219, 914

Berg, D. A., Pogge, R., Skillman, E., Moustakas, J., & Croxall, K. 2019, in preparation

Berg, D. A., Skillman, E. D., Croxall, K. V., Pogge, R. W., Moustakas, J., et al. 2015, ApJ, 806, 16

Binette, L., Matadamas, R., Hägele, G. F., et al. 2012, A&A, 547, A29

Bohlin, R. C. 2010, AJ, 139, 1515

Bresolin, F., Kudritzki, R.-P., Urbaneja, M. A., Gieren, W., Ho, I.-T., & Pietrzyński, G. 2016, ApJ, 830, 64

Bruzual, G. & Charlot, S. 2003, MNRAS, 344, 1000

Cardelli, J. A., Clayton, G. C., & Mathis, J. S. 1989, ApJ, 345, 245

Croxall, K. V. & Pogge, R. W. 2019, rwpogge/modsIDL: modsIDL Binocular Release [LINK]

Croxall, K. V., Pogge, R. W., Berg, D. A., Skillman, E. D., & Moustakas, J. 2015, ApJ, 808, 42

—. 2016, ApJ, 830, 4

Eldridge, J. J. & Stanway, E. R. 2016, MNRAS, 462, 3302

Esteban, C., Peimbert, M., García-Rojas, J., Ruiz, M. T., Peimbert, A., & Rodríguez, M. 2004, MNRAS, 355, 229

Esteban, C., Peimbert, M., Torres-Peimbert, S., & Escalante, V. 1998, MNRAS, 295, 401

Ferland, G. J., Porter, R. L., van Hoof, P. A. M., & others. 2013, , 49, 137

Fernandes, I. F., Gruenwald, R., & Viegas, S. M. 2005, MNRAS, 364, 674

Garcia-Rojas, J. & Esteban, C. 2006, arXiv Astrophysics e-prints

Garnett, D. R. 1992, AJ, 103, 1330

Guseva, N. G., Izotov, Y. I., Papaderos, P., & Fricke, K. J. 2007, A&A, 464, 885

Guseva, N. G., Izotov, Y. I., & Thuan, T. X. 2006, ApJ, 644, 890

Hägele, G. F., Pérez-Montero, E., Díaz, Á. I., Terlevich, E., & Terlevich, R. 2006, MNRAS, 372, 293

Hunter, J. D. 2007, Matplotlib: A 2D graphics environment

Johnson, J. A. 2019, Science, 363, 474 [LINK]

Jones, E., Oliphant, T., Peterson, P., et al. 2001–, SciPy: Open source scientific tools for Python, [Online; accessed March 29, 2019] [LINK]

Kelly, B. C. 2007, ApJ, 665, 1489

Liu, X.-W. & Danziger, J. 1993, MNRAS, 263, 256

Liu, X.-W., Luo, S.-G., Barlow, M. J., Danziger, I. J., & Storey, P. J. 2001, MNRAS, 327, 141

Lodders, K. 2010, Astrophysics and Space Science Proceedings, 16, 379

Maiolino, R. & Mannucci, F. 2019, A&A Rev., 27, 3

McCall, M. L. 2004, AJ, 128, 2144

McKinney, W. 2010, Data Structures for Statistical Computing in Python

Peimbert, A., Peimbert, M., & Ruiz, M. T. 2005, ApJ, 634, 1056

Peimbert, M. 1967, ApJ, 150, 825

—. 1971, Boletin de los Observatorios Tonantzintla y Tacubaya, 6, 29

Peimbert, M., Peimbert, A., Esteban, C., García-Rojas, J., Bresolin, F., Carigi, L., Ruiz, M. T., & López-Sánchez, A. R. 2007, in Revista Mexicana de Astronomia y Astrofisica, vol. 27, Vol. 29, Revista Mexicana de Astronomia y Astrofisica Conference Series, ed. R. Guzmán, 72–79

Pinsonneault, M. & Ryden, B. 2019, Stellar Structure and Evolution (The Ohio State University)

Pogge, R. W., Atwood, B., Brewer, D. F., et al. 2010, in Society of Photo-Optical Instrumentation Engineers (SPIE) Conference Series, Vol. 7735, Society of Photo-Optical Instrumentation Engineers (SPIE) Conference Series

Price-Whelan, A. M. et al. 2018, AJ, 156, 123

Ryden, B. & Pogge, R. 2016, Interstellar and Intergalactic Medium (The Ohio State University) [LINK]

Stanway, E. R., Eldridge, J. J., & Becker, G. D. 2016, MNRAS, 456, 485

Stasińska, G. Revista Mexicana de Astronomia y Astrofisica, vol. 27, Vol. 12, , Revista Mexicana de Astronomia y Astrofisica Conference Series, ed. W. J. HenneyJ. Franco & M. Martos, 62–69